Journal of Materials Chemistry

Cite this: J. Mater. Chem., 2012, 22, 2589

www.rsc.org/materials

PAPER

# Self-powered, visible-light photodetector based on thermally reduced graphene oxide–ZnO (rGO–ZnO) hybrid nanostructure†

**Zhaoyao Zhan, Lianxi Zheng,* Yongzheng Pan, Gengzhi Sun and Lin Li**

*Received 12th August 2011, Accepted 10th November 2011*
**DOI: 10.1039/c1jm13920g**



Here we report a new type of self-powered, visible-light photodetector fabricated from thermally reduced rGO–ZnO hybrid nanostructure. The photocurrent generation of the photodetectors under zero-bias enables hybrid rGO–ZnO devices to work like photovoltaic cells, which could power themselves without electrical power input. The thermal treatment at elevated temperature not only reduces graphene oxide (GO) into reduced graphene oxide (rGO), but also dopes the ZnO nanoparticles with carbon atoms, enabling their visible-light photoresponse capability. The pronounced and fast photocurrent generation was attributed to the efficient charge transfer between the rGO and carbon-doped ZnO nanoparticles, which were in intimate contact. The efficient charge transfer of the rGO–ZnO hybrid nanostructures also indicates that there could be applications in other light energy harvesting devices, including solar cells, sensors and visible-light photocatalysis.

## Introduction

Photodetection in the visible-light zone is of great importance for various applications including environmental and biological research, sensing, detection, and missile launch. There have been various kinds of commercial photodetectors fabricated from Si, Ge or other semiconductors. Photodetectors made from crystalline silicon are routinely used for imaging applications at visible and near-infrared wavelengths. The compatibility of silicon photodiodes with silicon electronics enables light sensing, low-noise electronic read out, multiplexing and so on. However, the high mobility and long lifetime of excitons in silicon lead to photocarrier diffusion, which can cause crosstalk and blurring of optical signals between neighboring pixels.[1] The high-temperature fabrication process is another concern for conventional crystalline Si photodetectors. Recently, the use of hybrid nanostructures in photodetectors has been an emerging research topic due to their high surface-to-volume ratio and also more freedom in the rational design of material properties. Currently, most of the photodetectors are operated based on sensing the changes in current or voltage of the device, but they need an electrical power input. A self-powered photodedector could operate under zero-bias without an extra power source. Several reported results on these zero-bias photodetectors are based on the photovoltaic effect.[2–6] The self-powered hybrid photodetector is especially desirable for astronautical exploration, since the extra weight of the electrical power source will dramatically increase launch cost.

Graphene, an atomic-layer-thick and two-dimensional system,[7] has triggered considerable research interest,[8,9] due to its fascinating electronic and mechanic properties prescribed by its unique structure.[10–12] The fascinating properties of graphene hold promising applications for gas sensors,[13,14] energy storage devices,[15] transparent electrodes[16] and ultrafast photodetectors.[17,18] However, the reported grapheme-based photodetectors can only work based on Schottky junctions at the contact interfacial area (around 2 μm wide), which is much smaller compared with the size of the whole devices. Since most of the area covered by the graphene between contacts could not contribute to the device performance, and graphene has poor light absorption in the visible zone, such devices have a very low sensitivity. To reach a full utilization of graphene's fascinating properties, a novel design using new structures or new materials is needed. At the same time, semiconductor nanoparticles (NPs) such as ZnO,[19–22] or CdE (E = S, Se, Te),[23–26] whose optical and electronic properties can be tuned by the size, shape and composition, have been intensively investigated in the past two decades. Thus it is of great interest to modify graphene sheets with such semiconductor NPs, because the combination of certain NPs with graphene might produce promising optoelectronic and energy conversion materials. For example, Wang *et al.*[27,28] have synthesized a reduced graphene oxide (rGO)–semiconductor NPs nanocomposite and found its interesting photovoltaic response and improved photoinduced-charge-transfer properties; Lin *et al.*[29] have reported synthesis of a rGO–CdSe hybrid and observed its dramatically enhanced photoresponse. In these materials, the excited electrons in the conduction band of semiconductor NPs will migrate into rGO, thereby decreasing the recombination possibility of electron–hole pairs.

*School of Mechanical and Aerospace Engineering, Nanyang Technological University, Nanyang Ave. 50, 639798, Singapore. E-mail: lxzheng@ntu.edu.sg; Tel: +65 6790 4163*

† Electronic supplementary information (ESI) available. See DOI: 10.1039/c1jm13920g

It is true that most of these narrow-gap semiconductors show excellent light absorption capability from the UV to the near infrared zone, however, the increasing environmental concerns with these materials (cadmium and lead) have turned us to more environment-friendly semiconductors, among which, ZnO has been widely investigated. Compared with Si photodetectors, ZnO-hybrid-nanostructured photodetectors have advantages in terms of small size, high breakdown electric field, high radiation resistance and wide operating temperature range.[3] The second advantage of ZnO-hybrid-nanostructured photodetectors is the low-temperature processing and large area integration.[1] In addition, the nanocrystals and hybrid nanostructures are readily synthesized in solution and tuned conveniently in terms of their size, shape, composition, and finally their optical and electronic properties. The low price and biocompatibility make ZnO nanocrystals or hybrid nanostructures more attractive.[2,3] The largest flaw with ZnO is the poor light absorption in the visible zone, due to its wide bandgap, and reported ZnO based hybrid photodetectors could only work in the UV zone.[30]

Countless endeavours have been devoted to extending the absorption of ZnO from the UV band to the visible zone. Various strategies, including atomic doping and surface modification by heterogeneous species, have been proposed to enhance the absorption of ZnO in the visible band. In particular, carbon doping method has been widely used to enhance the visible-light absorption of ZnO and improve its visible-light photocatalytic activity;[31] rGO was also used to enhance the photocatalytic activity of ZnO NPs.[32] Nevertheless, investigations of the visible-light photodetecting behaviour and photoinduced charge transfer behavior of carbon doped ZnO–rGO hybrid nanostructure are few.

Herein, we report ultrasensitive visible-light photoresponse of rGO–ZnO hybrid nanostructure synthesized by a solvothermal method then thermally reduced at 700 °C in Ar for 30 min. The thermal reduction process reduces graphene oxide (GO) into rGO, and dopes ZnO NPs with carbon atoms simultaneously. The carbon doping effectively extends the absorption of ZnO NPs to the visible light range. Thus, the rGO–ZnO hybrid photodetectors could present a significant response to visible light illumination under zero-bias, making the photodetectors self-powered. The distinct and fast photoresponse of the device is a direct result of enhanced charge transfer between rGO and ZnO NPs, as well as excellent electric properties of rGO sheets. This work will provide a new perspective on preparation and utilization of graphene–semiconductor nanocomposites for energy applications.

## Experimental section

### Synthesis of rGO–ZnO hybrid nanostructure

The hybrid nanostructure was prepared by a solvothermal method using GO as the template on which ZnO nanoparticles were grown. GO was prepared from graphite powder by a modified Hummers method.[33] The Zinc precursor for synthesis of both ZnO and rGO–ZnO was 0.2 M $Zn(Ac)_2 \cdot 2H_2O$ methanol solution. A typical synthesis process is as follows: first, 20 ml as-prepared 0.2 M $Zn(Ac)_2$ methanol solution was added into a 100 ml flask. Subsequently, 10 mg GO dispersed in 20 ml methanol was dropped into $Zn(Ac)_2$ methanol solution with vigorous stirring for 20 min to get uniform suspension. Then the flask was transferred to a 60 °C water bath and 40 ml 0.2 M KOH methanol solution was added into the flask dropwise over 10 min with intense stirring. Afterward, the mixture was maintained at 60 °C with stirring for two hours. At last, the flask was cooled to room temperature and placed in the dark overnight. The deposited products were washed with methanol and ethanol for several times to remove impurities, and were dried for further characterization. Then the as-synthesized products were thermally treated at 700 °C for 30 min with Ar gas as protection atmosphere. A control sample of carbon-doped ZnO-nanoparticle film was prepared following the same manner, but with less GO in solution.

### Characterization

The crystallographic information of the obtained products was determined using an X-ray diffractometer with Cu-K$\alpha$ radiation (Rigaku D/max-$\gamma$B, $\lambda = 0.15406$ nm). The morphology observation was conducted using a field emission scanning electron microscope (SEM, JEOL6340) and a transmission electron microscope (TEM, JEOL2100F, 200kV). Raman scattering of the hybrid nanostructures were collected on a Ranishaw inVia Raman microscope with an excitation laser of 514 nm. Absorption properties were investigated using a UV–vis spectrometer (Shimadzu UV-2450) with detecting range from 200 to 800 nm.

### Photodetecting tests

The as-prepared rGO–ZnO nanostructures were first dispersed into Isopropanol (IPA) by using soft ultrasonic stirring to get uniform suspension, and then spin-coated on a silicon substrate (with 500 nm oxide layer) patterned with gold electrodes (20 nm Ti/200 nm Au). Photoresponse tests were performed on a semiconductor parameter analyzer connected to a probe station. During the testing, the sampling period was set to 50 ms, and the variation in current of the photodetector with or without light illumination was recorded by the semiconductor parameter analyzer. A 400W Xenon lamp (AuLight, CEL-S500, Beijing, China) with an output window diameter of 5 cm was adopted as the light source, and the power density (white light) incident to the device surface is around 80 mW $cm^{-2}$. The 'On' and 'Off' of the illumination were controlled by a chopper. All of the above measurements were conducted in a dark room to minimize the influence of natural light.

## Results and discussion

### Characterization of rGO–ZnO hybrid nanostructure

Proper amount of rGO–ZnO products were dispersed in 2 ml ethanol with soft ultrasonic stirring for 30 min. The dispersed rGO–ZnO hybrid was then used for SEM and TEM observations. Fig. 1(a) shows a SEM image of thermally reduced rGO–ZnO hybrid. It is obvious that the rGO sheets are overlapped in a few layers, and ZnO particles are decorated on rGO randomly. TEM image of ZnO-decorated rGO–ZnO hybrid is shown in Fig. 1(b). The ZnO NPs have been successfully grown on the surface of rGO during the solvothermal process; the particle size

 

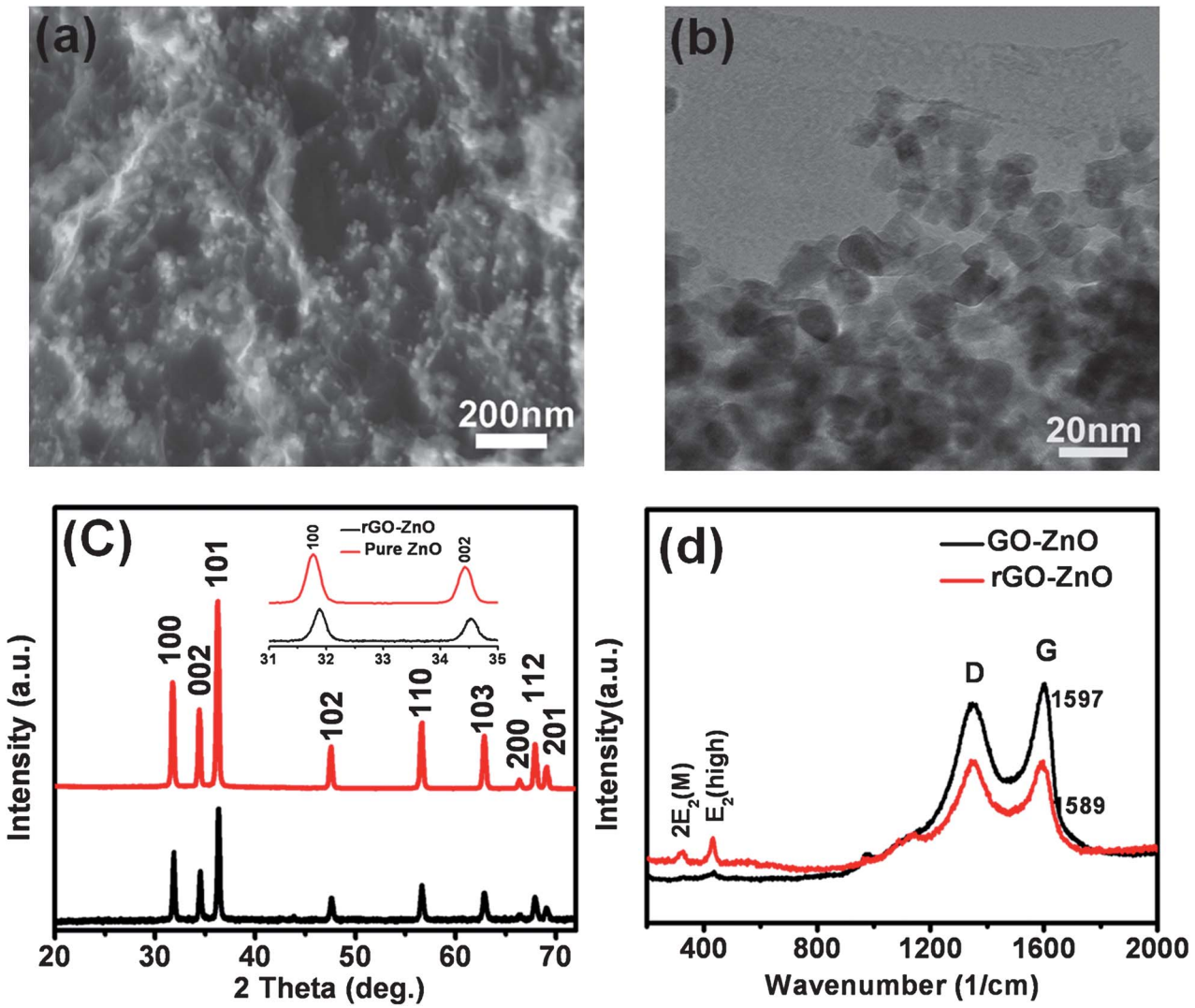


**Fig. 1** (a) SEM and (b) TEM images of the rGO–ZnO hybrid nanostructure; (c) XRD patterns of pure ZnO and rGO–ZnO hybrid, inset shows enlarged diffraction peaks at (100) and (002) planes; (d) Raman scattering spectra for GO–ZnO and rGO–ZnO hybrids.

is around 10 nm. XRD patterns of pure ZnO NPs and hybrid rGO–ZnO are compared in Fig. 1(c). The XRD pattern of pure ZnO nanoparticles corresponds to Wurtzite structured ZnO (JPCDS card No. 36-1451), whereas, the XRD pattern of rGO–ZnO hybrids show slight difference at the all diffraction planes. The inset in Fig. 1(c) shows enlarged diffraction patterns of (100) and (002) plane. Both diffraction peaks shift to larger angles after thermal reduction process, indicating that the lattice constant of ZnO in the rGO–ZnO hybrid becomes smaller. We attribute the lattice contraction to the carbon-doping-caused deformation of the ZnO lattice. Carbon doping effect on ZnO has been intensively investigated for applications in ferromagnetism[34,35] and photocatalysis[31] in past years. The carbon could substitute either Zn ($C_{Zn}$) or O ($C_O$) sites during the doping process, which depends on the calcination conditions.[31,36,37] In our case, as the GO–ZnO hybrid was calcined in Ar atmosphere, carbon atoms should substitute $Zn^{2+}$ vacancies to form $C_{Zn}$ defects, as suggested in other reported studies.[36,37] Since the size of $C^{4+}$ (0.15 Å) is smaller than $Zn^{2+}$ (0.77 Å), thus the substitution of $Zn^{2+}$ vacancy by $C^{4+}$ will lead to a contraction of the lattice around the defect sites, agreeing well with the XRD patterns.

Raman spectra of both GO–ZnO and rGO–ZnO hybrids are shown in Fig. 1(d). The peak at 328 $cm^{-1}$ is assigned to the $2E_2(M)$ mode of ZnO, and the one at 437 $cm^{-1}$ corresponds to the $E_2(high)$ vibration mode of ZnO. The peak at 1346 $cm^{-1}$ is the D band from the vibration of defect states in graphene sheets, and the peak in the vicinity of 1590 $cm^{-1}$ is assigned to the G band vibration of carbon materials. The G peak position of the original GO is located at 1597 $cm^{-1}$, after reduction the G peak shows a measurable red shift to 1589 $cm^{-1}$, which is also an indicator of GO reduction. Based on the above observation, we can conclude that the thermal reduction can reduce GO and dope ZnO simultaneously.

To further confirm this conclusion, X-ray photoelectron spectra (XPS) of both GO–ZnO (before reduction) and rGO–ZnO (after reduction) are collected, and shown in Fig. 2. In Fig. 2 (a), peaks located at 284.7, 285.5 and 288.7 eV are deconvolution spectra from C 1s of GO–ZnO, and correspond to C–C, C–OH,

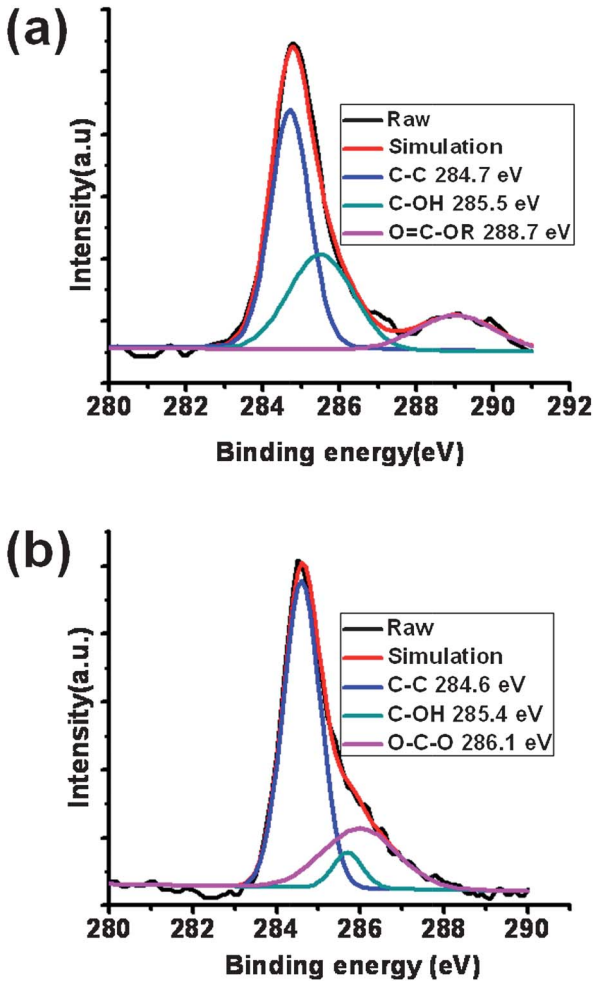


**Fig. 2** XPS spectra of C 1s in (a) as-prepared GO–ZnO; (b) rGO–ZnO hybrid.

and carboxylic groups O═C–OR, respectively. Fig. 2(b) shows C1s core spectra of rGO–ZnO hybrid. The peaks at 284.7, 285.5, and 286.1 eV are assigned to C–C, C–OH, and O–C–O, respectively. By comparing the XPS results of the GO–ZnO and rGO–ZnO hybrids, we find that GO has been reduced into rGO, and the presence of O–C–O in rGO–ZnO indicates that the doping of ZnO is due to the substitution of $Zn^{2+}$ by carbon atoms, which agrees well with above XRD observations and many other reported studies.[36,37]

## Optical properties

An indicator of the optical properties of rGO–ZnO hybrid nanostructure is the light absorption. Fig. 3 shows the light absorbance of both GO–ZnO and rGO–ZnO hybrids in the range from ultraviolet to the visible zone. The absorption peak at 370 nm of GO–ZnO is assigned to intrinsic band-edge absorption of ZnO NPs. By comparing the absorption of GO–ZnO and rGO–ZnO hybrids, we find that the absorption in the visible zone is substantially enhanced after thermal reduction. This enhancement in the visible light absorption could be mainly due to the carbon doping effect. The visible light absorption feature

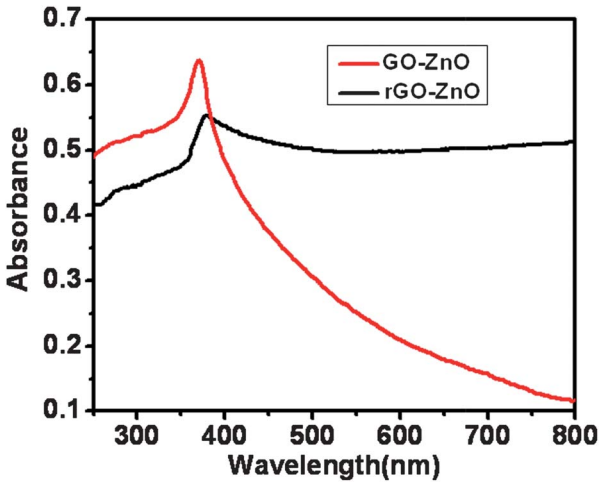


**Fig. 3** UV–vis absorption of GO–ZnO and rGO–ZnO hybrids.

of the rGO–ZnO hybrid nanostructure will have implications for its visible-light photodetecting capability.

## Photodetecting behaviour

In this section, we demonstrate that the rGO–ZnO hybrid couples the attractive properties of rGO and carbon-doped ZnO NPs, and could be used for energy conversion. As an initial step in this direction, photoconductivity and photocurrent generation of the rGO–ZnO hybrid films were tested upon exposure to light illumination in a wide wavelength range from UV to visible light. The schematic structure and testing setup of the hybrid rGO–ZnO photodetector are displayed in Scheme 1, and its photoresponse is shown in Fig. 4. From Fig. 4(a), we can observe a slight decrease of resistivity of the rGO–ZnO film after exposing to white light illumination. The slight decrease in resistivity (not a significant decrease as in most semiconductors) suggests that the conduction is dominated by the rGO sheets rather than ZnO particles, since rGO sheets have large surface and two-dimensional structure, which facilitate the connection between each other by either intra- or inter-layer connecting. Another interesting observation from Fig. 4(a) is the distinct electric current generated under zero-bias, indicating that this device could operate like a photovoltaic cell. There are several

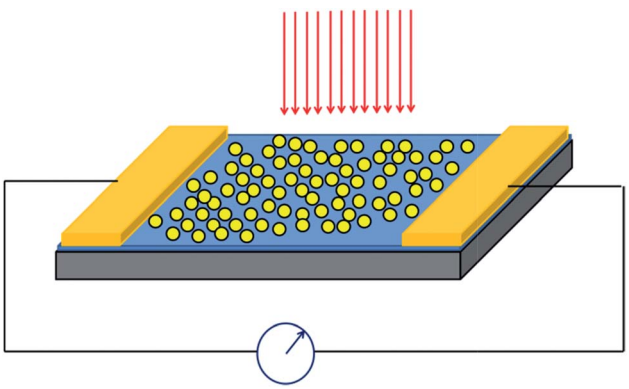

**Scheme 1** Schematic illustration of photodetecting test setup.

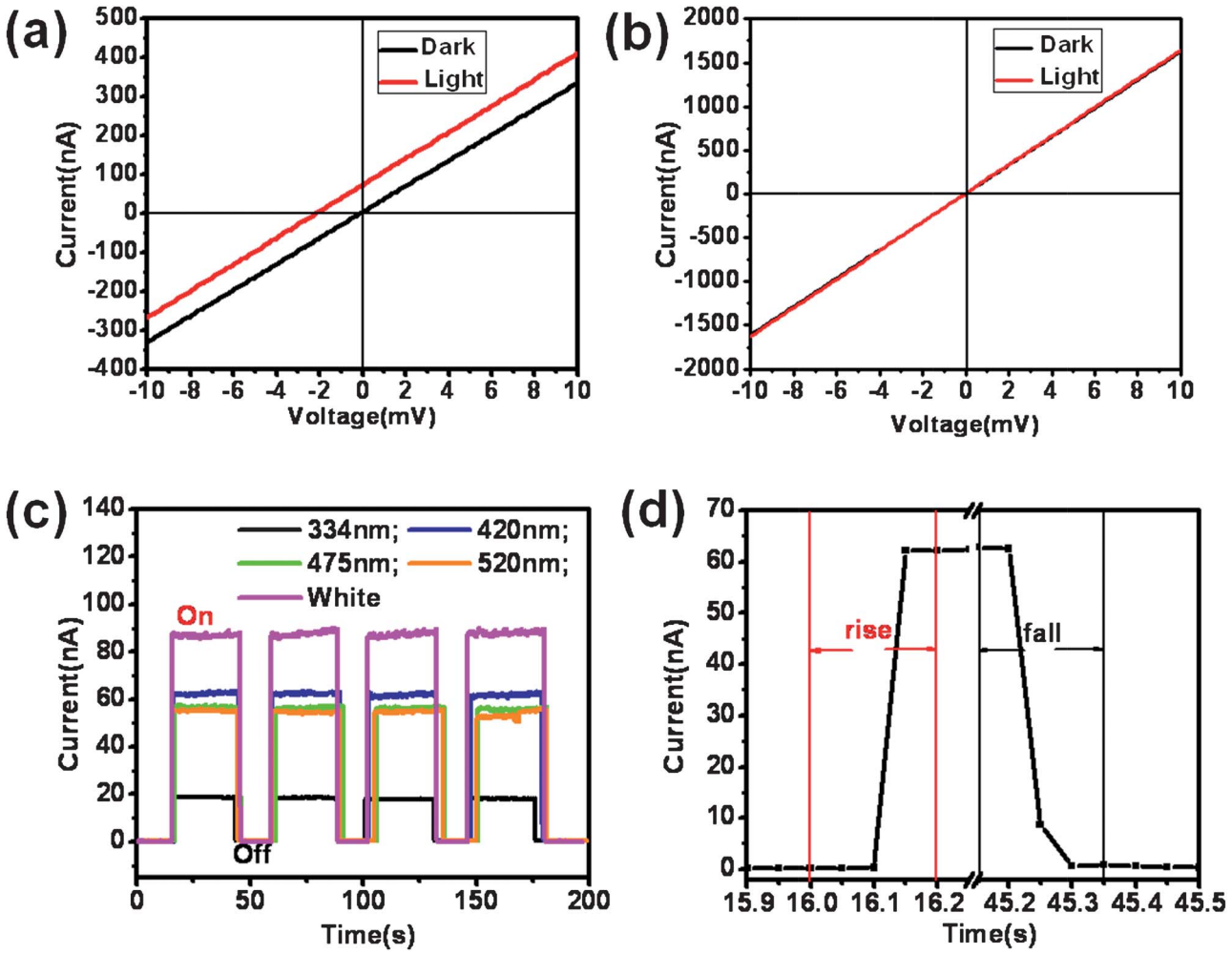


**Fig. 4** (a) *I–V* curves for the rGO–ZnO hybrid; (b) *I–V* curves for the pure rGO photodetector; (c) time-resolved photocurrent generation with illumination toggling between "on" and "off" for the rGO–ZnO photodector; (d) photoresponse dynamics of the hybrid rGO–ZnO photodetector.

reported works on the photoresponse behaviour of graphene devices, with Schottky junction formed at the contact interfacial area.[17] To check whether such a mechanism applies to our devices, we fabricated a control device using rGO (without ZnO), and measured its photoresponse behaviour at the same conditions. As displayed in Fig. 4(b), there is no measurable difference between the *I–V* characteristic curves with or without light illumination. The current–time course with light toggling between 'on' and 'off' does not show a well-defined photocurrent signal (data not shown). Thus the rGO alone could not generate a photocurrent signal in our device and measurement conditions. Therefore we attribute the photocurrent in Fig. 4(a) to the synergic effect of rGO and ZnO NPs.

To investigate the visible-light responsive behaviour of rGO–ZnO detectors, time-resolved photoresponse tests were conducted using Xenon light that is filtered by 334, 420, 475, and 550 nm band-pass filters, respectively, as the illumination source. The photocurrents shown in Fig. 4(c) were collected under zero-bias, with light illumination 'on' and 'off' controlled by a chopper. The pronounced photocurrent generated in the photodetector when illuminated by visible light demonstrates a strong visible-light photoresponse of the hybrid rGO–ZnO device.

Under white light illumination, the photoresponsivity defined by the ratio of photocurrent to dark current reached 430. This photoresponsivity is dramatically enhanced by 1500% compared the results in a recent report.[29] The response time is another indicator of performance of a photodetector. As displayed in Fig. 4(c), the current will ramp to its steady value instantly once the photodetector is exposed to illumination. The response time of this photodetector can be extracted from the current–time course curves in Fig. 4(d). Both rise and fall times are less than 0.2 s, which indicates a fast response of the photodetector. Previously most of reported UV photodetectors based on pure ZnO nanostructures exhibitd a response time ranging from seconds to minutes.[38,39] As suggested by Thong *et al.*, the photoresponse characteristics of ZnO are significantly influenced by many factors including defect concentration, crystallographic orientation, grain size and processing conditions.[40] In our experiments, the rapid response of this rGO–ZnO hybrid could be attributed to the intimate contact between the rGO sheets and ZnO NPs, which enables a fast charge transfer and dissipation of carriers.[41]

Since the ZnO particles with Schottky contact could also give zero-bias photocurrent, we have conducted a set of control

experiments on carbon-doped ZnO–nanoparticle devices (without rGO to facilitate the charge transfer and transport). The *I–V* characteristic curves (Fig. S1†) of carbon-doped ZnO–nanoparticle device under dark and illumination condition show Schottky contact, and a measurable 2 nA photocurrent signal under zero-bias, which is much lower than that of rGO–ZnO hybrid devices. The response time (Fig. S2†) of cabon-doped ZnO–nanoparticle devices is also much longer than that of rGO–ZnO hybrid devices: it takes about 1 s to raise the spike peak, and more than 20 s to reach its steady state. These poor performances are reasonable, considering that only the excitons in the Schottky contact area could be effectively separated, and they must be transported through a hopping mechanism. These results further confirm that the photoresponse in our rGO–ZnO devices is a synergic effect of rGO and ZnO: effective charge transfer between their interface and fast charge transport by rGO.

## Mechanisms

As mentioned earlier, previous reported studies of graphene photodetection indicate that the Schottky junction formed at the contact interfacial area is critical for the photocurrent generation.[17,42] But in our devices, such contact area (either with ZnO or rGO) doesn't contribute very much to the photocurrent generation (supported by the performance of the pure rGO device in Fig. 4(b) and control device in Fig. S1–S2†). To further elucidate the response mechanism of our devices, an *in situ* photoresponse test was conducted by utilizing a ×50 microscope objective lens to focus a laser beam (514 nm laser) into a 2 μm spot, and also by a microstage to control the spot position. Fig. 5(a) shows schematics of the experimental setup. The laser spot could be located at any position on the device surface, ranging from the contact areas at both sides to the middle area in between. When the laser spot was focused at a middle position, that is from 5 to 10 μm from the contact areas at both sides, with the laser toggling between 'on' and 'off', the device will give a distinct current signal, increasing from background (2 pA) to a stable value (around 20 pA), as shown in Fig. 5(b). The *in situ* photoresponse behaviour at the contact interfacial area (around 2 μm distance from the contact) is almost the same as that of the middle area. Based on these *in situ* studies, we can assure that the photoresponse mechanism in our case should be different from those for reported graphene photodetecting devices, in which the photocurrent originated from the exciton dissociation by the Schottky junction formed at the contact interfacial area.[17,42] The photocurrent in our device should be from the charge transfer process between rGO sheets and carbon-doped ZnO NPs.

Reported studies of ZnO and its hybrid nanostructures' photoresponses suggested that ambient $O_2$ adsorbs on ZnO surfaces and traps free electrons from n-type ZnO.[38,39,41,43,44] When the device is illuminated by photons with energy higher than the band gap of ZnO (around 3.37 eV), electron–hole pairs will be generated in ZnO NPs. The photo-generated holes will migrate to the particle surface and discharge the adsorbed $O_2^-$ ions. The remaining free electrons will enhance the conductivity of ZnO or transfer to the attached matrix, as schematically illustrated in

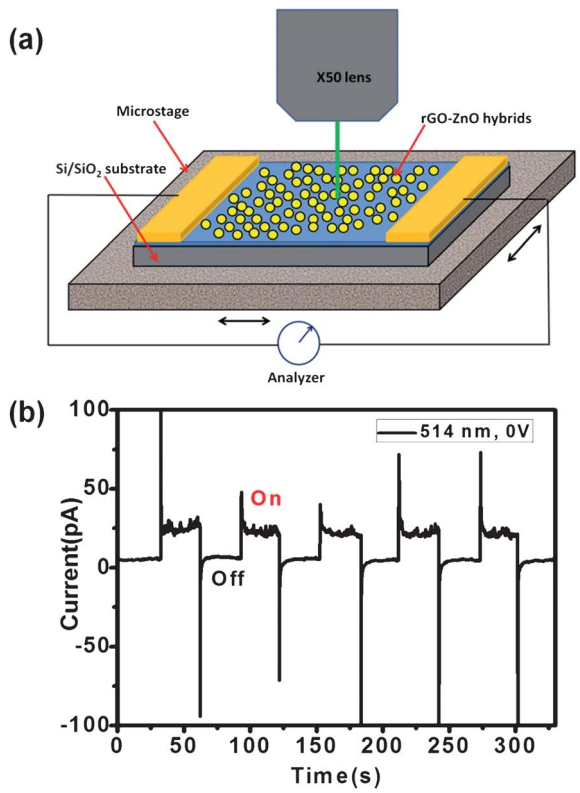


**Fig. 5** (a) Schematic of *in situ* measurement set-up; (b) time-resolved photocurrent generation with illumination toggling between "on" and "off".

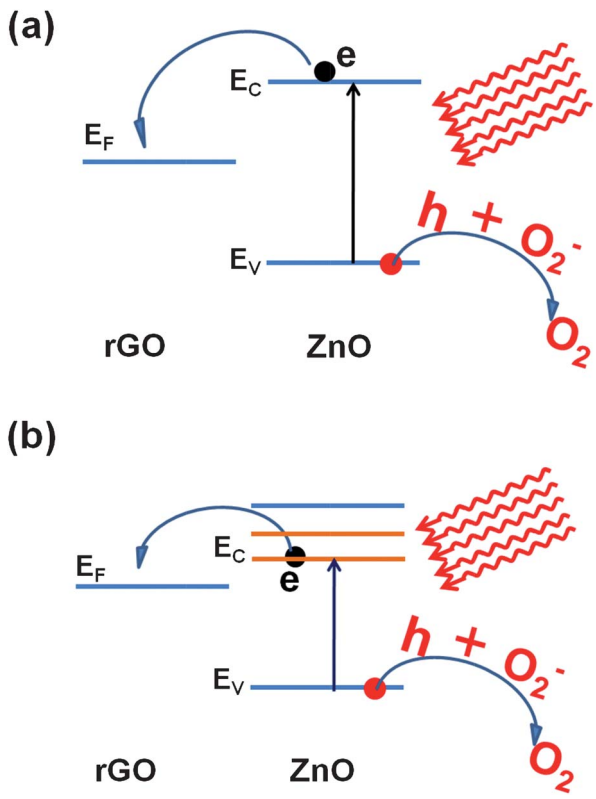


**Fig. 6** Schematic illustration of charge transfer process involving oxygen-adsorption upon illumination of (a) undoped ZnO–rGO hybrid, (b) carbon-doped ZnO–rGO hybrid, the brown lines denote new energy levels generated by carbon doping.

Fig. 6(a). In our experiment, the high temperature reduction process dopes the ZnO (as indicated by XPS results) and introduces new energy levels in the forbidden gap, thereby narrowing its band gap. The UV–vis absorption result of the rGO–ZnO hybrid further confirms the doping of ZnO NPs, extending the absorption from the UV zone to the visible zone. Thus, visible light illumination could also excite electrons to the new energy levels in the carbon-doped ZnO NPs and cause a continuous oxygen-mediated turnover process in hybrid rGO–ZnO devices, as depicted in Fig. 6(b). Continuous adsorption and desorption of ionized surface oxygen will trap photogenerated holes, while free electrons will be transferred into the rGO layer and then transported to the electrode, and thus a distinct photocurrent is generated under zero bias.

## Conclusions

We have demonstrated a facile method to fabricate self-powered, visible-light photodetectors based on a thermally reduced rGO–ZnO hybrid nanostructure. The visible-light photoresponse is due to the carbon doping of ZnO during the thermal reduction process, which also reduces GO into rGO. The photocurrent generation under zero bias is a result of fast charge transfer at rGO–ZnO interfaces and effective charge transport in rGO sheets, together with continuous adsorption and desorption of ionized surface oxygen. This feature implies that a rGO–ZnO photodetector could operate like a photovoltaic cell, *i.e.* it could power itself under light illumination. The excellent charge transfer capability and visible light response make the thermally reduced rGO–ZnO hybrid material a good candidate for applications in photodetection, sensors, and photocatalysis.

## Acknowledgements

One of the authors, Zhaoyao Zhan, wants to thank Dr Yajun Qi for his kind help with SEM and TEM characterization, and also to thank PhD student Fengji Li for his help with XPS experiments.

## References

1 G. Konstantatos and E. H. Sargent, *Nat. Nanotechnol.*, 2010, **5**, 391–400.
2 H. Zhu, C. X. Shan, B. Yao, B. H. Li, J. Y. Zhang, D. X. Zhao, D. Z. Shen and X. W. Fan, *J. Phys. Chem. C*, 2008, **112**, 20546–20548.
3 H. Zhu, C. X. Shan, L. K. Wang, J. Zheng, J. Y. Zhang, B. Yao and D. Z. Shen, *J. Phys. Chem. C*, 2010, **114**, 7169–7172.
4 J. K. Sheu, M. L. Lee, C. J. Tun and S. W. Lin, *Appl. Phys. Lett.*, 2006, **88**, 043506.
5 F. Sun, C. X. Shan, S. P. Wang, B. H. Li, Z. Z. Zhang, C. L. Yang and D. Z. Shen, *Mater. Chem. Phys.*, 2011, **129**, 27–29.
6 C. Yang, X. M. Li, W. D. Yu, X. D. Gao, X. Cao and Y. Z. Li, *J. Phys. D: Appl. Phys.*, 2009, **42**, 152002.
7 K. S. Novoselov, A. K. Geim, S. V. Morozov, D. Jiang, Y. Zhang, S. V. Dubonos, I. V. Grigorieva and A. A. Firsov, *Science*, 2004, **306**, 666–669.
8 C. Lee, X. D. Wei, J. W. Kysar and J. Hone, *Science*, 2008, **321**, 385–388.
9 A. K. Geim and K. S. Novoselov, *Nat. Mater.*, 2007, **6**, 183–191.
10 S. Stankovich, D. A. Dikin, G. H. B. Dommett, K. M. Kohlhaas, E. J. Zimney, E. A. Stach, R. D. Piner, S. T. Nguyen and R. S. Ruoff, *Nature*, 2006, **442**, 282–286.
11 K. S. Novoselov, A. K. Geim, S. V. Morozov, D. Jiang, M. I. Katsnelson, I. V. Grigorieva, S. V. Dubonos and A. A. Firsov, *Nature*, 2005, **438**, 197–200.
12 A. H. Castro Neto, F. Guinea, N. M. R. Peres, K. S. Novoselov and A. K. Geim, *Rev. Mod. Phys.*, 2009, **81**, 109–162.
13 F. Schedin, A. K. Geim, S. V. Morozov, E. W. Hill, P. Blake, M. I. Katsnelson and K. S. Novoselov, *Nat. Mater.*, 2007, **6**, 652–655.
14 J. D. Fowler, M. J. Allen, V. C. Tung, Y. Yang, R. B. Kaner and B. H. Weiller, *ACS Nano*, 2009, **3**, 301–306.
15 H. Gwon, H. S. Kim, K. U. Lee, D. H. Seo, Y. C. Park, Y. S. Lee, B. T. Ahn and K. Kang, *Energy Environ. Sci.*, 2011, **4**, 1277–1283.
16 X. Wang, L. J. Zhi and K. Mullen, *Nano Lett.*, 2008, **8**, 323–327.
17 F. N. Xia, T. Mueller, Y. M. Lin, A. Valdes-Garcia and P. Avouris, *Nat. Nanotechnol.*, 2009, **4**, 839–843.
18 T. Mueller, F. N. A. Xia and P. Avouris, *Nat. Photonics*, 2010, **4**, 297–301.
19 V. A. Fonoberov and A. A. Balandin, *Appl. Phys. Lett.*, 2004, **85**, 5971–5973.
20 R. Viswanatha, S. Sapra, B. Satpati, P. V. Satyam, B. N. Dev and D. D. Sarma, *J. Mater. Chem.*, 2004, **14**, 661–668.
21 V. A. Fonoberov and A. A. Balandin, *J. Nanoelectron. Optoelectron.*, 2006, **1**, 19–38.
22 V. A. Fonoberov, K. A. Alim, A. A. Balandin, F. X. Xiu and J. L. Liu, *Phys. Rev. B*, 2006, 73.
23 C. B. Murray, D. J. Norris and M. G. Bawendi, *J. Am. Chem. Soc.*, 1993, **115**, 8706–8715.
24 A. P. Alivisatos, *J. Phys. Chem.*, 1996, **100**, 13226–13239.
25 X. G. Peng, L. Manna, W. D. Yang, J. Wickham, E. Scher, A. Kadavanich and A. P. Alivisatos, *Nature*, 2000, **404**, 59–61.
26 A. P. Alivisatos, *Science*, 1996, **271**, 933–937.
27 P. Wang, T. F. Jiang, C. Z. Zhu, Y. M. Zhai, D. J. Wang and S. J. Dong, *Nano Res.*, 2010, **3**, 794–799.
28 P. Wang, Y. M. Zhai, D. J. Wang and S. J. Dong, *Nanoscale*, 2011, **3**, 1640–1645.
29 Y. Lin, K. Zhang, W. F. Chen, Y. D. Liu, Z. G. Geng, J. Zeng, N. Pan, L. F. Yan, X. P. Wang and J. G. Hou, *ACS Nano*, 2010, **4**, 3033–3038.
30 H. X. Chang, Z. H. Sun, K. Y. F. Ho, X. M. Tao, F. Yan, W. M. Kwok and Z. J. Zheng, *Nanoscale*, 2011, **3**, 258–264.
31 S. Cho, J. W. Jang, J. S. Lee and K. H. Lee, *CrystEngComm*, 2010, **12**, 3929–3935.
32 T. G. Xu, L. W. Zhang, H. Y. Cheng and Y. F. Zhu, *Appl. Catal., B*, 2011, **101**, 382–387.
33 W. S. Hummers and R. E. Offeman, *J. Am. Chem. Soc.*, 1958, **80**, 1339–1339.
34 H. Pan, J. B. Yi, L. Shen, R. Q. Wu, J. H. Yang, J. Y. Lin, Y. P. Feng, J. Ding, L. H. Van and J. H. Yin, *Phys. Rev. Lett.*, 2007, 99.
35 X. J. Ye, C. S. Liu, W. Zhong, H. A. Song, C. T. Au and Y. W. Du, *Phys. Lett. A*, 2010, **374**, 496–500.
36 S. Akbar, S. K. Hasanain, M. Abbas, S. Ozcan, B. Ali and S. I. Shah, *Solid State Commun.*, 2011, **151**, 17–20.
37 S. T. Tan, X. W. Sun, Z. G. Yu, P. Wu, G. Q. Lo and D. L. Kwong, *Appl. Phys. Lett.*, 2007, **91**, 072101.
38 H. Kind, H. Q. Yan, B. Messer, M. Law and P. D. Yang, *Adv. Mater.*, 2002, **14**, 158–160.
39 C. Soci, A. Zhang, B. Xiang, S. A. Dayeh, D. P. R. Aplin, J. Park, X. Y. Bao, Y. H. Lo and D. Wang, *Nano Lett.*, 2007, **7**, 1003–1009.
40 J. B. K. Law and J. T. L. Thong, *Appl. Phys. Lett.*, 2006, **88**, 133114.
41 J. G. Ok, S. H. Tawfick, K. A. Juggernauth, K. Sun, Y. Y. Zhang and A. J. Hart, *Adv. Funct. Mater.*, 2010, **20**, 2470–2480.
42 E. J. H. Lee, K. Balasubramanian, R. T. Weitz, M. Burghard and K. Kern, *Nat. Nanotechnol.*, 2008, **3**, 486–490.
43 Y. Z. Jin, J. P. Wang, B. Q. Sun, J. C. Blakesley and N. C. Greenham, *Nano Lett.*, 2008, **8**, 1649–1653.
44 S. Liu, J. F. Ye, Y. Cao, Q. Shen, Z. F. Liu, L. M. Qi and X. F. Guo, *Small*, 2009, **5**, 2371–2376.